

# Improved search for two-neutrino double electron capture on $^{124}\text{Xe}$ and $^{126}\text{Xe}$ using particle identification in XMASS-I

XMASS Collaboration\*

K. Abe<sup>1,5</sup>, K. Hiraide<sup>1,5</sup>, K. Ichimura<sup>1,5</sup>, Y. Kishimoto<sup>1,5</sup>, K. Kobayashi<sup>1,5</sup>, M. Kobayashi<sup>1</sup>, S. Moriyama<sup>1,5</sup>, M. Nakahata<sup>1,5</sup>, T. Norita<sup>1</sup>, H. Ogawa<sup>1,5</sup>, K. Sato<sup>1</sup>, H. Sekiya<sup>1,5</sup>, O. Takachio<sup>1</sup>, A. Takeda<sup>1,5</sup>, S. Tasaka<sup>1</sup>, M. Yamashita<sup>1,5</sup>, B. S. Yang<sup>1,5</sup>, N. Y. Kim<sup>2</sup>, Y. D. Kim<sup>2</sup>, Y. Itow<sup>3,6</sup>, K. Kanzawa<sup>3</sup>, R. Kegasa<sup>3</sup>, K. Masuda<sup>3</sup>, H. Takiya<sup>3</sup>, K. Fushimi<sup>4,†</sup>, G. Kanzaki<sup>4</sup>, K. Martens<sup>5</sup>, Y. Suzuki<sup>5</sup>, B. D. Xu<sup>5</sup>, R. Fujita<sup>7</sup>, K. Hosokawa<sup>7,†</sup>, K. Miuchi<sup>7</sup>, N. Oka<sup>7</sup>, Y. Takeuchi<sup>7,5</sup>, Y. H. Kim<sup>8,2</sup>, K. B. Lee<sup>8</sup>, M. K. Lee<sup>8</sup>, Y. Fukuda<sup>9</sup>, M. Miyasaka<sup>10</sup>, K. Nishijima<sup>10</sup>, S. Nakamura<sup>11</sup>

<sup>1</sup>*Kamioka Observatory, Institute for Cosmic Ray Research, the University of Tokyo, Higashi-Mozumi, Kamioka, Hida, Gifu 506-1205, Japan*

<sup>2</sup>*Center of Underground Physics, Institute for Basic Science, 70 Yuseong-daero 1689-gil, Yuseong-gu, Daejeon 305-811, South Korea*

<sup>3</sup>*Institute for Space-Earth Environmental Research, Nagoya University, Nagoya, Aichi 464-8601, Japan*

<sup>4</sup>*Institute of Socio-Arts and Sciences, The University of Tokushima, 1-1 Minamijosanjimacho Tokushima city, Tokushima, 770-8502, Japan*

<sup>5</sup>*Kavli Institute for the Physics and Mathematics of the Universe (WPI), the University of Tokyo, Kashiwa, Chiba 277-8582, Japan*

<sup>6</sup>*Kobayashi-Maskawa Institute for the Origin of Particles and the Universe, Nagoya University, Furo-cho, Chikusa-ku, Nagoya, Aichi 464-8602, Japan*

<sup>7</sup>*Department of Physics, Kobe University, Kobe, Hyogo 657-8501, Japan*

<sup>8</sup>*Korea Research Institute of Standards and Science, Daejeon 305-340, South Korea*

<sup>9</sup>*Department of Physics, Miyagi University of Education, Sendai, Miyagi 980-0845, Japan*

<sup>10</sup>*Department of Physics, Tokai University, Hiratsuka, Kanagawa 259-1292, Japan*

<sup>11</sup>*Department of Physics, Faculty of Engineering, Yokohama National University, Yokohama, Kanagawa 240-8501, Japan*

\*E-mail: [xmass.publications7@km.icrr.u-tokyo.ac.jp](mailto:xmass.publications7@km.icrr.u-tokyo.ac.jp)

.....  
 We conducted an improved search for the simultaneous capture of two  $K$ -shell electrons on the  $^{124}\text{Xe}$  and  $^{126}\text{Xe}$  nuclei with emission of two neutrinos using 800.0 days of data from the XMASS-I detector. A novel method to discriminate  $\gamma$ -ray/ $X$ -ray or double electron capture signals from  $\beta$ -ray background using scintillation time profiles was developed for this search. No significant signal was found when fitting the observed energy spectra with the expected signal and background. Therefore, we set the most stringent lower limits on the half-lives at  $2.1 \times 10^{22}$  and  $1.9 \times 10^{22}$  years for  $^{124}\text{Xe}$  and  $^{126}\text{Xe}$ , respectively, with 90% confidence level. These limits improve upon previously reported values by a factor of 4.5.  
 .....

## 1. Introduction

Double electron capture (ECEC) is a rare nuclear decay process where a nucleus captures two orbital electrons simultaneously. There might be two modes of the process:

$$(Z, A) + 2e^- \rightarrow (Z - 2, A) , \quad (1)$$

$$(Z, A) + 2e^- \rightarrow (Z - 2, A) + 2\nu_e , \quad (2)$$

where  $Z$  and  $A$  are the atomic number and atomic mass number of the nucleus, respectively.

Detecting the neutrinoless mode of this process ( $0\nu$ ECEC) would provide evidence for lepton number violation and the Majorana nature of the neutrino if observed. To release the decay energy in  $0\nu$ ECEC, there are two proposed mechanisms: the radiative and the resonant mechanisms. In the case of the radiative mechanism, the decay energy is carried away by emitting, for example, an internal Bremsstrahlung photon [1, 2]. This process is, however, expected to have a much longer life-time than neutrinoless double beta decay. On the other hand, an enhancement of the capture rate by a factor as large as  $10^6$  is possible if the initial and final (excited) masses of the nucleus are degenerate [3–8]. Therefore, experimental searches for  $0\nu$ ECEC have been recently performed for a variety of candidate nuclei [9–19].

Although two-neutrino double electron capture ( $2\nu$ ECEC) is allowed within the Standard Model of particle physics, only a few positive experimental results for  $2\nu$ ECEC have been reported: geochemical measurements of  $^{130}\text{Ba}$  [22, 23] and a direct measurement of  $^{78}\text{Kr}$  [19, 24] with half-lives of the order of  $10^{21}$ – $10^{22}$  years. Despite the nuclear matrix element for the two-neutrino mode differs from that for the neutrinoless mode, they are related to each other through the relevant parameters in a chosen nuclear model [25]. For instance, the nucleus' axial current coupling constant  $g_A$  and the strength of the particle-particle interaction  $g_{pp}$  in the quasiparticle random-phase approximation (QRPA) model are obtained from single  $\beta$ -decay and two-neutrino double beta decay measurements [26]. Measurements of the  $2\nu$ ECEC half-lives with various nuclei would shed new light on constraining these parameters.

Natural xenon contains  $^{124}\text{Xe}$  (abundance 0.095%) and  $^{126}\text{Xe}$  (0.089%), in which ECEC can be observed.  $^{124}\text{Xe}$  has the highest  $Q$ -value among all the known candidate nuclei for ECEC at 2864 keV [27]. This  $Q$ -value is sufficiently large to open the  $\beta^+\text{EC}$  and  $\beta^+\beta^+$  channels. The predictions in the literature for the half-lives of  $^{124}\text{Xe}$   $2\nu$ ECEC are spread over a wide range between  $10^{20}$  and  $10^{24}$  years [21, 28–32] depending on the models used for calculating the corresponding nuclear matrix element and the effective value of the nucleus'  $g_A$ . Although  $^{126}\text{Xe}$  can also undergo  $2\nu$ ECEC, the life-time of this process for  $^{126}\text{Xe}$  is expected to be much longer than that for  $^{124}\text{Xe}$  since its  $Q$ -value is smaller at 920 keV [27].

Previous experimental searches for  $2\nu$ ECEC on  $^{124}\text{Xe}$  have sought the simultaneous capture of two  $K$ -shell electrons ( $2\nu 2K$ ) using a gas proportional counter with enriched xenon and large-volume liquid xenon (LXe) detectors with natural xenon as the target.

---

<sup>†</sup>Now at Department of Physics, Tokushima University, 2-1 Minami Josanjimacho Tokushima city, Tokushima, 770-8506, Japan

<sup>‡</sup>Now at Research Center for Neutrino Science, Tohoku University, Sendai, Miyagi 980-8578, Japan

**Table 1** Summary of experimental searches for two-neutrino double electron capture on  $^{124}\text{Xe}$  reported to date compared with this work.

Experiment	$^{124}\text{Xe}$ target mass (g)	live time	$T_{1/2}^{2\nu 2K} (^{124}\text{Xe})$ ( $10^{21}$ years)
XMASS (This work)	311	800.0 days	$> 21$
XMASS [37]	39	132.0 days	$> 4.7$
Gavrilyuk <i>et al.</i> [34]	58.6	3220 h	$> 2.0$
XENON100 [38]	29	224.6 days	$> 0.65$

An experiment with a proportional counter containing 58.6 g of  $^{124}\text{Xe}$  (enriched to 23%) published the latest lower bound on the half-life,  $T_{1/2}^{2\nu 2K} (^{124}\text{Xe}) > 2.0 \times 10^{21}$  years at 90% confidence level (CL) [33, 34]. Large-volume LXe detectors can also observe  $2\nu\text{ECEC}$  on  $^{124}\text{Xe}$  [35, 36]. The XMASS experiment has conducted a search with a fiducial xenon mass of 41 kg (containing 39 g of  $^{124}\text{Xe}$ ) and set the most stringent lower limit of  $T_{1/2}^{2\nu 2K} (^{124}\text{Xe}) > 4.7 \times 10^{21}$  years [37]. The XENON100 experiment also published a result obtained with a fiducial xenon mass of 34 kg (containing about 29 g of  $^{124}\text{Xe}$ ) and set a lower limit of  $T_{1/2}^{2\nu 2K} (^{124}\text{Xe}) > 6.5 \times 10^{20}$  years [38]. These searches were conducted with similar amount of  $^{124}\text{Xe}$  and live time as summarized in Table 1. In addition, the XMASS experiment set the first experimental lower limit on the  $^{126}\text{Xe}$   $2\nu 2K$  half-life at  $T_{1/2}^{2\nu 2K} (^{126}\text{Xe}) > 4.3 \times 10^{21}$  years using the same data set.

In this paper, we report the results of an improved search for  $^{124}\text{Xe}$  and  $^{126}\text{Xe}$   $2\nu 2K$  events, using data from the XMASS-I detector. We analyze a new data set taken between November 2013 and July 2016. The total live time amounts to 800.0 days and the fiducial xenon mass was enlarged to 327 kg (containing about 311 g of  $^{124}\text{Xe}$ ). We developed a novel method for discriminating the  $2\nu 2K$  signal from the  $\beta$ -ray background using LXe scintillation time profiles.

## 2. The XMASS-I detector

XMASS-I is a large single-phase LXe detector located underground (2700 m water equivalent) at the Kamioka Observatory in Japan [39]. An active target of 832 kg of LXe is held inside a pentakis-dodecahedral copper structure that hosts 642 inward-looking 2-inch Hamamatsu R10789 photomultiplier tubes (PMTs) on its approximately spherical inner surface at a radius of about 40 cm. The photocathode coverage of the inner surface is 62.4%. Signals from each PMT are recorded with CAEN V1751 waveform digitizers with a sampling rate of 1 GHz and 10-bit resolution.

The gains of the PMTs are monitored weekly using a blue LED embedded in the inner surface of the detector. The scintillation yield response is traced with a  $^{57}\text{Co}$  source [40] inserted along the central vertical axis of the detector every week or two. Through measurements with the  $^{57}\text{Co}$  source at the center of the detector volume, the photoelectron (PE) yield was determined to be  $\sim 15$  PE/keV for 122 keV  $\gamma$ -rays. The nonlinear response of the scintillation yield for electron-mediated events in the detector was calibrated over the energy range from 5.9 keV to 2614 keV with  $^{55}\text{Fe}$ ,  $^{241}\text{Am}$ ,  $^{109}\text{Cd}$ ,  $^{57}\text{Co}$ ,  $^{137}\text{Cs}$ ,  $^{60}\text{Co}$ , and  $^{232}\text{Th}$  sources. Hereinafter, this calibrated energy is represented as  $\text{keV}_{ee}$  where the subscript

---

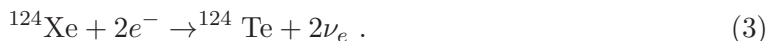
stands for the electron-equivalent energy. The timing offsets for the PMT channels owing to the differences in their cable lengths and the electronic responses were also traced by the  $^{57}\text{Co}$  calibration.

The LXe detector is located at the center of a cylindrical water Cherenkov detector, which is 11 m in height and 10 m in diameter. The outer detector is equipped with 72 20-inch Hamamatsu H3600 PMTs. This detector acts as an active veto counter for cosmic-ray muons as well as a passive shield against neutrons and  $\gamma$ -rays from the surrounding rock.

Data acquisition is triggered if at least four inner-detector PMTs record a signal within 200 ns or if at least eight outer-detector PMTs register a signal within 200 ns. A 50 MHz clock is used to measure the time difference between triggers. One-pulse-per-second (1PPS) signals from the global positioning system (GPS) are fed as triggers for precise time stamping. The GPS 1PPS triggers are also used to flash the LED for the PMT gain monitoring.

### 3. Expected signal and simulation

The process of  $2\nu\text{ECEC}$  on  $^{124}\text{Xe}$  is



If two  $K$ -shell electrons in the  $^{124}\text{Xe}$  atom are captured simultaneously, a daughter atom of  $^{124}\text{Te}$  is formed with two vacancies in the  $K$ -shell and this atom relaxes by emitting atomic  $X$ -rays and/or Auger electrons. Our Monte Carlo simulations of the atomic de-excitation signal are based on the atomic relaxation package in Geant4 [41]. On the assumption that the  $X$ -rays and Auger electrons emitted in the  $2\nu 2K$  event are like those generated by two single  $K$ -shell vacancies, the signal simulation begins with two Te atoms with a single  $K$ -shell vacancy. In such a case, the total energy deposition is given by twice the  $K$ -shell binding energy of Te ( $2K_b = 63.63$  keV). On the other hand, the energy of the two electron holes in the  $K$ -shell of  $^{124}\text{Te}$  is calculated to be 64.46 keV [42], which only varies by 0.8 keV. Since the energy resolution of the  $2\nu 2K$  signal peak is estimated to be 3.2 keV after all the detector responses mentioned below are accounted for, we judge that this difference is negligible in our analysis. The results actually do not change even if the peak position of the simulated signal is artificially shifted by this amount. According to the simulation, 77% of  $2\nu 2K$  events emit two  $K$ -shell  $X$ -rays, 21% of events emit a single  $K$ -shell  $X$ -ray, and the remaining 1.6% of events emits no  $K$ -shell  $X$ -ray. These probabilities are consistent with those expected from the fluorescence yield for the  $K$ -shell of Te,  $\omega_K = 0.875$  [43]. Auger electron cascades are also simulated. The energy deposition from the recoil of the daughter nucleus is  $\sim 30$  eV at most, which is negligible. Simulated de-excitation events are generated uniformly throughout the detector volume.

The nonlinearity of scintillation yield is accounted for using the nonlinearity model from Doke et al. [44] with a further correction obtained from the  $\gamma$ -ray calibrations. The absolute energy scale of the simulation is adjusted at 122 keV. The time profile of the scintillation is also modeled based on the  $\gamma$ -ray calibrations [45]. Propagation of scintillation photons in LXe is also simulated. Optical parameters of the LXe such as absorption and scattering lengths for the scintillation are tuned by source calibration data at various positions. The group velocity of the scintillation light in the LXe follows from LXe's refractive index ( $\sim 11$  cm/ns for 175-nm light [46]). Charge and timing responses of the PMTs are also modeled in the simulation based on the calibrations with the LED and the  $\gamma$ -ray sources. Finally, waveforms

---

**Table 2** Summary of the data set used in this analysis.

Period	Start date–End date	Live time (days)	Gas circulation	Comment
1	Nov 20, 2013–May 13, 2014	124.0	None	Activated
2	May 13, 2014–Mar 13, 2015	249.1	None	
3	Mar 13, 2015–Mar 29, 2016	338.1	~1.5 L/min	
4	Apr 14, 2016–Jul 20, 2016	88.8	~1.5 L/min	Activated

of the PMT signal are simulated using the template of a single-PE waveform obtained from the LED calibration data.

#### 4. Data set

The data used in the present analysis were collected between November 20, 2013 and July 20, 2016. The data set was divided into four periods depending on the detector conditions at that time as summarized in Table 2. Period 1 started two weeks after the introduction of LXe into the detector. At the beginning of the run, we observed neutron-activated peaks from  $^{131\text{m}}\text{Xe}$  and  $^{129\text{m}}\text{Xe}$  that were created when the LXe was stored outside the water shield. We also performed the  $^{252}\text{Cf}$  calibration data collection twice in this period. Runs within 10 days after each calibration were excluded from the data set. We ended period 1 60 days after the second  $^{252}\text{Cf}$  calibration because the  $^{131\text{m}}\text{Xe}$  and  $^{129\text{m}}\text{Xe}$  peaks caused by the  $^{252}\text{Cf}$  disappeared. Period 2 then ran until the continuous gas circulation at a flow rate of  $\sim 1.5$  L/min with a getter purifier was introduced. Period 3 was ended so that the xenon could be purified by vaporizing xenon once to remove possible non-volatile impurities dissolved in LXe. During the purification process, LXe was extracted from the detector, and therefore, xenon was exposed to and activated by thermal neutrons outside the water shield. The purification process took 7 days and period 4 started immediately after completing the introduction of LXe into detector.

We selected periods of operation under what we call normal data taking conditions with a stable temperature (172.6–173.0 K) and pressure (0.162–0.164 MPa absolute) of the LXe in the detector. After further removing periods of operation that include excessive PMT noise, unstable pedestal levels, or abnormal trigger rates, the total live time became 800.0 days.

#### 5. Event reduction and classification

The event-reduction process comprises four steps: pre-selection, the fiducial volume selection,  $^{214}\text{Bi}$  identification, and particle identification.

##### 5.1. Pre-selection

Pre-selection requires that no outer-detector trigger is associated with an event, that the time elapsed since the previous inner-detector event ( $dT_{\text{pre}}$ ) is at least 10 ms, and that the standard deviation of the inner-detector hit timing distribution in the event is less than 100 ns. The last two requirements remove events caused by after-pulses in the PMTs following bright events. The  $dT_{\text{pre}}$  cut eliminates events by chance coincidence at a probability of 3.0% on average, which was estimated from the fraction of the GPS 1PPS events that are rejected

---

by this cut. The chance coincidence probability is counted as dead time, and the live time mentioned above is obtained after subtracting this dead time.

### 5.2. Fiducial volume selection

To select events that occurred within the fiducial volume, an event vertex is reconstructed based on a maximum-likelihood evaluation of the observed light distribution in the detector [39]. We select events whose reconstructed vertex has a radial distance of less than 30 cm from the center of the detector. The fiducial mass of natural xenon in that volume is 327 kg, containing 311 g of  $^{124}\text{Xe}$  and 291 g of  $^{126}\text{Xe}$ .

### 5.3. $^{214}\text{Bi}$ identification

$^{222}\text{Rn}$  emanates from the detector's surface and contaminates the LXe within the detector. Thus, its daughters,  $^{214}\text{Bi}$  and  $^{214}\text{Pb}$ , become one of the major sources of  $\beta$ -ray background.  $^{214}\text{Bi}$  can be tagged using the  $^{214}\text{Bi}$ - $^{214}\text{Po}$  delayed coincidence ( $T_{1/2} = 164 \mu\text{s}$ ) and is used as a good control sample of pure  $\beta$ -ray events in the relevant energy range. To remove the  $^{214}\text{Bi}$  events, events whose time difference from the subsequent event ( $dT_{\text{post}}$ ) is less than 1 ms are rejected from the  $2\nu 2\text{K}$  signal sample. This cut reduces the  $^{214}\text{Bi}$  background by a factor of  $\sim 70$ , while consequently discarding only 0.4% of all other events. The counterpart sample, *i.e.* events with  $0.015 \text{ ms} < dT_{\text{post}} < 1 \text{ ms}$ , is referred to as the  $^{214}\text{Bi}$  sample and is used to constrain the  $^{214}\text{Bi}$  and  $^{214}\text{Pb}$  backgrounds.

### 5.4. Particle identification

The scintillation time profiles of LXe can be used for particle identification. We use them to eliminate both the  $\alpha$ -ray and  $\beta$ -ray backgrounds from the  $2\nu 2\text{K}$  signal sample.

After the fiducial volume selection, the largest source of background in the relevant energy range are  $\beta$ -rays coming from radioactive impurities within the LXe.  $2\nu 2\text{K}$  or  $\gamma$ -ray events can be discriminated from these  $\beta$ -ray events by utilizing the energy dependence of the scintillation decay time for electron-induced events. The scintillation decay time increases from 28 ns to 48 ns as the kinetic energy of an electron increases from 3 keV to 1 MeV as summarized in Fig. 3 of [45]. In the case of the  $2\nu 2\text{K}$  or  $\gamma$ -ray events, the X-ray or  $\gamma$ -ray is converted into multiple low-energy electrons in the LXe; this shortens the effective scintillation decay time by a few ns from that of an event caused by a single electron with the same deposited energy. Especially, events caused by  $2\nu 2\text{K}$  or  $\gamma$ -rays with energy close to twice of the  $K$ -shell binding energy are easily-distinguishable from the  $\beta$ -ray events by this effective scintillation decay time.

The particle-identification parameter  $\beta\text{CL}$  is formulated as follows. First, waveforms in each PMT are decomposed into single-PE pulses using the single-PE waveform template [45]. Figure 1 shows an example of a waveform recorded in a PMT from the  $^{241}\text{Am}$  calibration data. Decomposed single-PE pulses are also shown in the figure. The timings of the decomposed single-PE pulses in all the PMTs are sorted chronologically after correcting for the time-of-flight of scintillation photons. The single-PE pulses in the first 20 ns are excluded from the following calculation to avoid systematic uncertainties in the leading edge of the

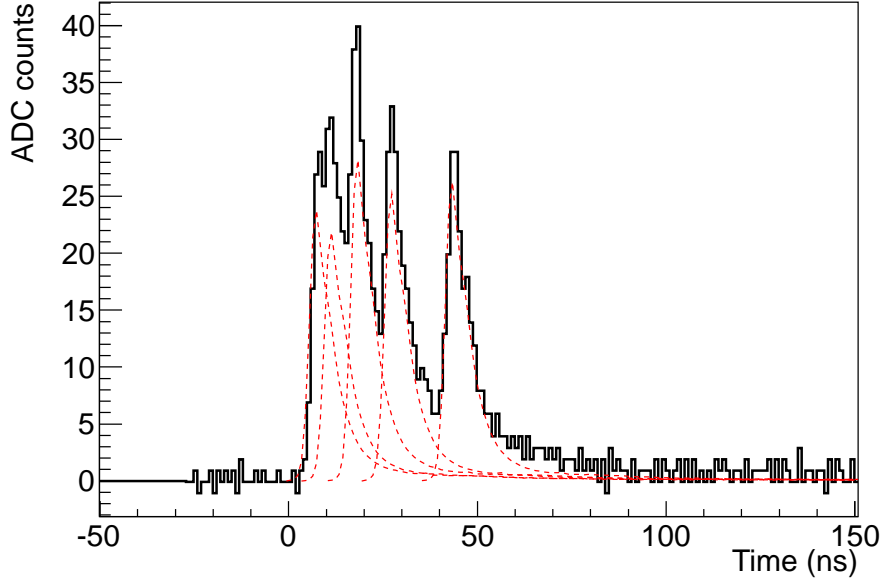


**Fig. 1** An example waveform recorded in a PMT from the  $^{241}\text{Am}$  calibration data. The  $^{241}\text{Am}$  source was placed at  $z = 20$  cm. Red dashed curves represent decomposed single-PE pulses.

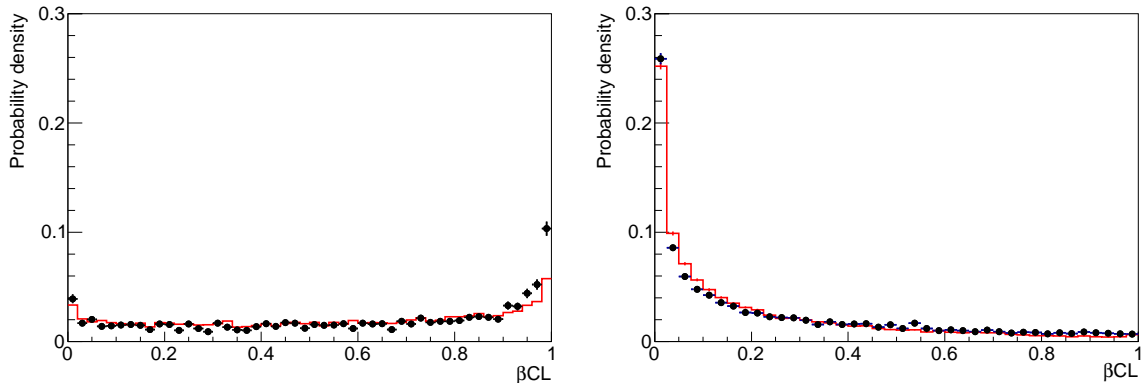
scintillation time profile. The variable  $\beta\text{CL}$  is defined as

$$\beta\text{CL} = P \times \sum_{i=0}^{n-1} \frac{(-\ln P)^i}{i!}, \quad (4)$$

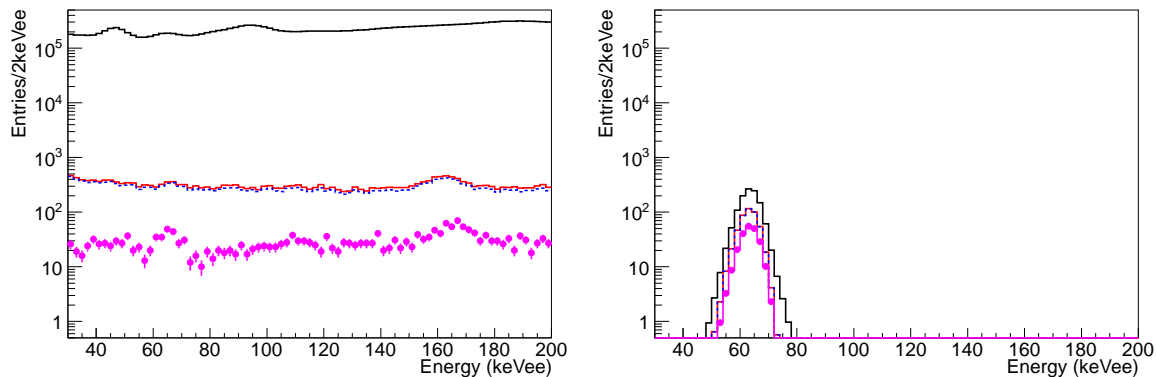
where  $n$  is the total number of single-PE pluses after truncating the first 20 ns,  $P = \prod_{i=0}^{n-1} \text{CL}_i$ , and  $\text{CL}_i$  ( $i=0, 1, 2, \dots, n-1$ ) is the CL of each pulse timing under the assumption that the event is caused by a  $\beta$ -ray. The probability-density function of the pulse-timing distribution for a  $\beta$ -ray event including its energy and position dependences is modeled from measurements in the  $^{214}\text{Bi}$  data sample over the energy range between 30 and 200  $\text{keV}_{\text{ee}}$ . This formula is in general used to combine  $p$ -values from a set of independent tests for a certain hypothesis [47].

Figure 2 shows distributions of the variable  $\beta\text{CL}$  for the  $^{214}\text{Bi}$  sample in the energy range from 30 to 200  $\text{keV}_{\text{ee}}$  along with the  $^{241}\text{Am}$  59.5 keV  $\gamma$ -ray events. While the  $\beta$ -ray events in the  $^{214}\text{Bi}$  sample are distributed between 0 and 1, the distribution of the 59.5 keV  $\gamma$ -ray events in the  $^{241}\text{Am}$  sample peaks at  $\beta\text{CL} = 0$ . Events with  $\beta\text{CL}$  less than 0.05 are classified as the  $\beta$ -depleted sample, and the rest is referred to as the  $\beta$ -enriched sample. When selecting events with  $\beta\text{CL}$  less than 0.05, 42% of the  $2\nu 2\text{K}$  signal events are selected, while only 6% of the  $\beta$ -ray events from the  $^{214}\text{Bi}$  decay in this energy range are selected. Thus, the signal-to-noise ratio is improved by a factor of 7 by this selection. The cut position is tuned based on the simulated data to maximize the sensitivity for the  $2\nu 2\text{K}$  signal.

$\alpha$ -ray events often occur in the grooves of the inner surface of the detector, so that only some of their energy is detected. These events are sometimes incorrectly reconstructed within the fiducial volume [48]. Above 30  $\text{keV}_{\text{ee}}$ ,  $\alpha$ -ray events can be clearly separated from  $\beta$ -ray



**Fig. 2** The particle-identification parameter  $\beta\text{CL}$  for the  $^{214}\text{Bi}$   $\beta$ -ray events in the energy range from 30 to 200  $\text{keV}_{\text{ee}}$  (left) and the  $^{241}\text{Am}$  59.5  $\text{keV}$   $\gamma$ -ray events (right). The distributions of the observed data (black points) and the simulated events (red curves) are normalized to the unit area.



**Fig. 3** Energy spectra after each event reduction step for the observed data (left) and the simulated  $2\nu 2\text{K}$  sample assuming  $T_{1/2} = 4.7 \times 10^{21}$  years (right). From top to bottom, energy distributions after the pre-selection (black solid), fiducial volume selection (red solid),  $^{214}\text{Bi}$  rejection (blue dashed nearly overlaps with red solid), and  $\beta$ -like event rejection (magenta points) steps are shown.

or  $\gamma$ -ray events using the scintillation decay time. Therefore, the waveforms from all PMTs are summed up to form a total waveform of the event after correcting for the relative gain and timing of each PMT. Then, the falling edge of that total waveform is fitted with an exponential function to obtain the decay time for each event. Events with fitted decay times of less than 30 ns are deemed  $\alpha$ -ray events and are rejected.

Figure 3 shows the energy spectra plotted after each event-reduction step for the observed data and the simulated  $2\nu 2\text{K}$  sample. For the simulated  $2\nu 2\text{K}$  sample,  $T_{1/2} = 4.7 \times 10^{21}$  years is assumed.



## 6. Spectrum fitting

### 6.1. Chi-square definition

To extract the  $2\nu 2K$  signal from the observed data, the energy spectra for the  $\beta$ -depleted samples,  $\beta$ -enriched samples, and  $^{214}\text{Bi}$  samples are simultaneously fitted to the expected signal and background spectra. The energy range from 30 to 200 keV<sub>ee</sub> is used for fitting. The chi-square value is defined as

$$\begin{aligned}\chi^2 &= -2 \ln L \\ &= 2 \sum_{i=1}^{N_{\text{sample}}} \sum_{j=1}^{N_{\text{period}}} \sum_{k=1}^{N_{\text{bin}}} \left( n_{ijk}^{\text{exp}}(p_l) - n_{ijk}^{\text{data}} + n_{ijk}^{\text{data}} \ln \frac{n_{ijk}^{\text{data}}}{n_{ijk}^{\text{exp}}(p_l)} \right) + \sum_{l=1}^{N_{\text{sys}}} \frac{(1 - p_l)^2}{\sigma_l^2}, \quad (5)\end{aligned}$$

where  $n_{ijk}^{\text{data}}$ , and  $n_{ijk}^{\text{exp}}(p_l)$  are the observed and expected number of events in  $i$ -th sub-sample and  $j$ -th period and  $k$ -th energy bin, respectively.  $N_{\text{sample}} = 3$ ,  $N_{\text{period}} = 4$ ,  $N_{\text{bin}} = 85$ , and  $N_{\text{sys}}$  are the number of sub-samples, periods, energy bins, and constrained systematic parameters, respectively.  $p_l$  and  $\sigma_l$  are a scaling parameter for the nominal value and its relative error, respectively.

### 6.2. Expected background

We consider three types of backgrounds: radioactive isotopes (RIs) in the LXe, neutron activation of xenon, and external backgrounds.

For the internal RIs, the  $^{222}\text{Rn}$  daughters ( $^{214}\text{Bi}$  and  $^{214}\text{Pb}$ ),  $^{85}\text{Kr}$ ,  $^{39}\text{Ar}$ ,  $^{14}\text{C}$ , and  $^{136}\text{Xe}$  are considered. The  $^{214}\text{Bi}$  activity during each period is determined from the fitting to the  $^{214}\text{Bi}$  sample and the  $^{214}\text{Pb}$  activity in each period follows from this  $^{214}\text{Bi}$  activity as both originate from  $^{222}\text{Rn}$ . While  $^{85}\text{Kr}$  decays by  $\beta$ -decay ( $Q_\beta = 687$  keV,  $T_{1/2} = 10.8$  years) predominantly into the ground state of  $^{85}\text{Rb}$ , 0.434% of their decays go into the 514-keV excited state of  $^{85}\text{Rb}$  followed by a nuclear relaxation  $\gamma$ -ray ( $T_{1/2} = 1.014$   $\mu\text{s}$ ).  $^{85}\text{Kr}$  contamination in the detector is measured to be  $0.26 \pm 0.06$  mBq by the coincidence of  $\beta$ -ray and  $\gamma$ -ray events. In this analysis, the  $^{85}\text{Kr}$  activity in each period is fitted with this constraint. We have also found argon contamination in the xenon through measurements of the sampled xenon gas using gas chromatography-mass spectrometry (GC-MS). The argon is thought to have adsorbed to the detector material when we conducted a leakage test of the LXe chamber using argon gas in 2013.  $^{39}\text{Ar}$  undergoes  $\beta$ -decay ( $Q_\beta = 565$  keV,  $T_{1/2} = 269$  years). By comparing the energy spectra for periods 2 and 3 of the data set, we found a reduction in event rate below  $\sim 150$  keV<sub>ee</sub> in the  $\beta$ -enriched sample. The difference in the energy spectra between two periods is consistent with the  $\beta$ -decay of  $^{14}\text{C}$  ( $Q_\beta = 156$  keV,  $T_{1/2} = 5730$  years). Hence, we assume that impurities containing carbon were reduced by gas circulation through the getter although its chemical form is not known. Finally, natural xenon contains  $^{136}\text{Xe}$  with an isotopic abundance of 8.9%, and  $^{136}\text{Xe}$  undergoes  $2\nu\beta\beta$  decay ( $Q_{\beta\beta} = 2.46$  MeV,  $T_{1/2} = 2.2 \times 10^{21}$  years [49, 50]).

Although the LXe detector is shielded against environmental neutrons by water, some of the detector components such as the cable feed-through box, calibration system, and cryogenic system lie outside the water shield and are filled with xenon gas [39]. The volume of xenon gas outside the water shield is estimated to be  $2.6 \times 10^5$  cm<sup>3</sup> at the standard temperature of 273.15 K and pressure of  $10^5$  Pa. This xenon is activated by thermal neutron capture and returned to the LXe in the detector. The resulting 13 RIs,  $^{125}\text{Xe}$ ,  $^{125\text{m}}\text{Xe}$ ,  $^{125}\text{I}$ ,

**Table 3** Summary of systematic parameters and their uncertainties used as constraints in the spectrum fitting.

Item	Fractional uncertainty	Period dependence
$^{222}\text{Rn}$ daughters ( $^{214}\text{Bi}$ and $^{214}\text{Pb}$ )	Unconstrained	Assumed
$^{85}\text{Kr}$	$\pm 23\%$	Assumed
$^{39}\text{Ar}$	Unconstrained	Assumed
$^{14}\text{C}$	Unconstrained	Assumed
Thermal neutron flux	$\pm 27\%$	Assumed
Additional $^{131\text{m}}\text{Xe}$	Unconstrained	Assumed
Additional $^{133}\text{Xe}$	Unconstrained	Assumed
$\gamma$ -ray backgrounds from PMTs	$\pm 9.4\%$ ( $^{238}\text{U}$ ), $\pm 24\%$ ( $^{232}\text{Th}$ ), $\pm 11\%$ ( $^{60}\text{Co}$ ), $\pm 17\%$ ( $^{40}\text{K}$ )	Not assumed
Isotopic abundance	$\pm 8.5\%$ ( $^{124}\text{Xe}$ ), $\pm 12\%$ ( $^{126}\text{Xe}$ )	Not assumed
Fiducial volume	$\pm 4.5\%$	Not assumed
$\beta\text{CL}$ acceptance for $\gamma$ -ray	$\pm 30\%$	Not assumed
$\beta\text{CL}$ acceptance for $\beta$ -ray	$\pm 8.0\%$	Not assumed
Energy scale ( $\beta$ -depleted sample)	$\pm 2.0\%$	Assumed
Energy scale ( $\beta$ -enriched sample)	$\pm 2.0\%$	Assumed

$^{127}\text{Xe}$ ,  $^{127\text{m}}\text{Xe}$ ,  $^{129\text{m}}\text{Xe}$ ,  $^{131\text{m}}\text{Xe}$ ,  $^{133}\text{Xe}$ ,  $^{133\text{m}}\text{Xe}$ ,  $^{135}\text{Xe}$ ,  $^{135\text{m}}\text{Xe}$ ,  $^{137}\text{Xe}$ , and  $^{137}\text{Cs}$ , are also considered. Their activities are calculated based on the isotopic abundance of xenon and the cross sections of thermal neutron capture. Among those isotopes,  $^{125}\text{I}$  is the most considerable background in this analysis. The  $^{125}\text{I}$  is produced from  $^{125}\text{Xe}$  and  $^{125\text{m}}\text{Xe}$  created by thermal neutron capture on  $^{124}\text{Xe}$  with a total cross section of  $165 \pm 11$  barn [51].  $^{125}\text{I}$  decays by 100% electron capture via an excited state of  $^{125}\text{Te}$  into the ground state of  $^{125}\text{Te}$  with a total energy deposition of 67.5 keV. The flux of thermal neutrons ( $E < 0.5$  eV) in the Kamioka mine has been measured to be  $(0.8\text{-}1.4) \times 10^{-5}$  / $\text{cm}^2/\text{s}$  [52, 53]. In this analysis, the thermal neutron flux during each period is fitted under the constraint of these measurements.  $^{125}\text{I}$ ,  $^{131\text{m}}\text{Xe}$ , and  $^{133}\text{Xe}$  are the main RIs relevant to this analysis and the entire energy range of the beta-depleted samples has the power to constrain the thermal neutron flux. Activations of xenon by neutrons emitted from the  $(\alpha, n)$  reaction or spontaneous fission in the detector material is negligible. In addition, occasional neutron activations of the LXe appear in periods 1 and 4 due to the  $^{252}\text{Cf}$  calibration and the purification works. The data taken just after the  $^{252}\text{Cf}$  calibration, which were excluded from this analysis, showed clear event rate increases in the energy range between 30 and 200 keV due to  $^{131\text{m}}\text{Xe}$  and  $^{133}\text{Xe}$ . To accommodate these backgrounds, we introduce additional quantities of  $^{131\text{m}}\text{Xe}$  and  $^{133}\text{Xe}$  in the fitting.

For the external backgrounds, a detailed evaluation of radioactive backgrounds from each detector material has been conducted previously [48]. In the present data set, a small contribution of  $\gamma$ -ray backgrounds from impurities in the PMTs is expected.  $^{238}\text{U}$ ,  $^{232}\text{Th}$ ,  $^{60}\text{Co}$ , and  $^{40}\text{K}$  are considered, and the uncertainties in their activities are accounted for in the fitting.

---

### 6.3. Systematic uncertainties

Systematic uncertainties in the background yields, exposure, event selections, and energy scales are considered in the fitting as listed in Table 3. The upper part of Table 3 summarizes the systematic parameters used to determine the activities of RI backgrounds in the spectrum fitting. The  $^{85}\text{Kr}$  activity, thermal neutron flux, and  $\gamma$ -ray backgrounds from the PMTs are constrained by the external measurements as described in the previous section since this spectrum fitting does not have the sensitivity for an independent evaluation.

Isotopic composition of the LXe was measured with a mass spectrometer, and the result was consistent with that of natural xenon in air [37]. The uncertainties in the measurement,  $\pm 8.5\%$  for  $^{124}\text{Xe}$  and  $\pm 12\%$  for  $^{126}\text{Xe}$ , are treated as a systematic error. The uncertainties in the LXe density and the detector live time are negligible. The uncertainties in the event selections and energy scales are estimated from comparisons between data and simulated samples for the  $^{241}\text{Am}$  (59.5 keV  $\gamma$ -ray) and  $^{57}\text{Co}$  (122 keV  $\gamma$ -ray) calibration data at various positions within the fiducial volume. The radial position of the reconstructed vertex for the calibration data differs from that for the simulated result by  $\pm 4.5$  mm near the fiducial volume boundary, which causes  $\pm 4.5\%$  uncertainty in the fiducial LXe volume. From the difference in the  $\beta\text{CL}$  distribution between the calibration data and simulated samples, the uncertainty in acceptance of the  $\beta\text{CL}$  cut for the  $\gamma$ -ray events is found to be  $\pm 30\%$ . In the same manner, the uncertainty in the rejection power of the  $\beta\text{CL}$  cut for  $\beta$ -ray events is evaluated to be  $\pm 8.0\%$  from the comparison of the  $\beta\text{CL}$  distributions for the  $^{214}\text{Bi}$  sample in the energy range from 30 to 200 keV<sub>ee</sub>. By comparing the peak position of the  $\gamma$ -ray calibration data and simulated samples at various source positions and in different periods, the uncertainty in energy scale for the  $\gamma$ -ray events is estimated to be  $\pm 2.0\%$ . Since we observe a small difference in the peak position of the  $\gamma$ -ray calibration data between the  $\beta$ -depleted and  $\beta$ -enriched samples, the energy scales for the  $\beta$ -depleted and  $\beta$ -enriched samples are treated independently.

## 7. Results and discussion

Figure 4 shows the energy spectra for the  $\beta$ -depleted samples,  $\beta$ -enriched samples, and  $^{214}\text{Bi}$  samples. The observed spectra are overlaid with the best-fit  $2\nu 2\text{K}$  signal and background spectra. The best fit result gives  $\chi^2/\text{ndf} = 1073/999$ . The bottom figures determine the activities of  $^{214}\text{Bi}$  in LXe and constrain the  $^{214}\text{Pb}$  activities. The middle figures determine the  $^{39}\text{Ar}$  and  $^{14}\text{C}$  activities while the amount of  $^{85}\text{Kr}$  is constrained by the independent  $\beta$ - $\gamma$  coincidence measurement. The variation in time of the fitted activities of  $^{214}\text{Bi}$ ,  $^{85}\text{Kr}$ ,  $^{39}\text{Ar}$ , and  $^{14}\text{C}$  in the active 832 kg LXe volume are shown in Fig. 5. The  $^{222}\text{Rn}$  concentration in LXe increased by  $\sim 50\%$  after gas circulation was initiated at the beginning of period 3. It is surmised that  $^{222}\text{Rn}$  emanating from detector materials in the xenon gas volume mixes into the LXe by the gas circulation. An increase of the  $^{39}\text{Ar}$  concentration in period 3 is thought to occur in the same manner. On the other hand, the  $^{14}\text{C}$  concentration decreased with gas circulation.

Figure 6 shows the variation in time of the fitted thermal neutron flux, additional activities of  $^{131\text{m}}\text{Xe}$  and  $^{133}\text{Xe}$  in the active 832 kg LXe volume, and energy scales. The fitted thermal neutron flux is stable over the entire data set at  $\sim 8 \times 10^{-6}$  /cm<sup>2</sup>/s. The larger amounts of  $^{131\text{m}}\text{Xe}$  in periods 1 and 4 are explained by the neutron activation of LXe while storing the

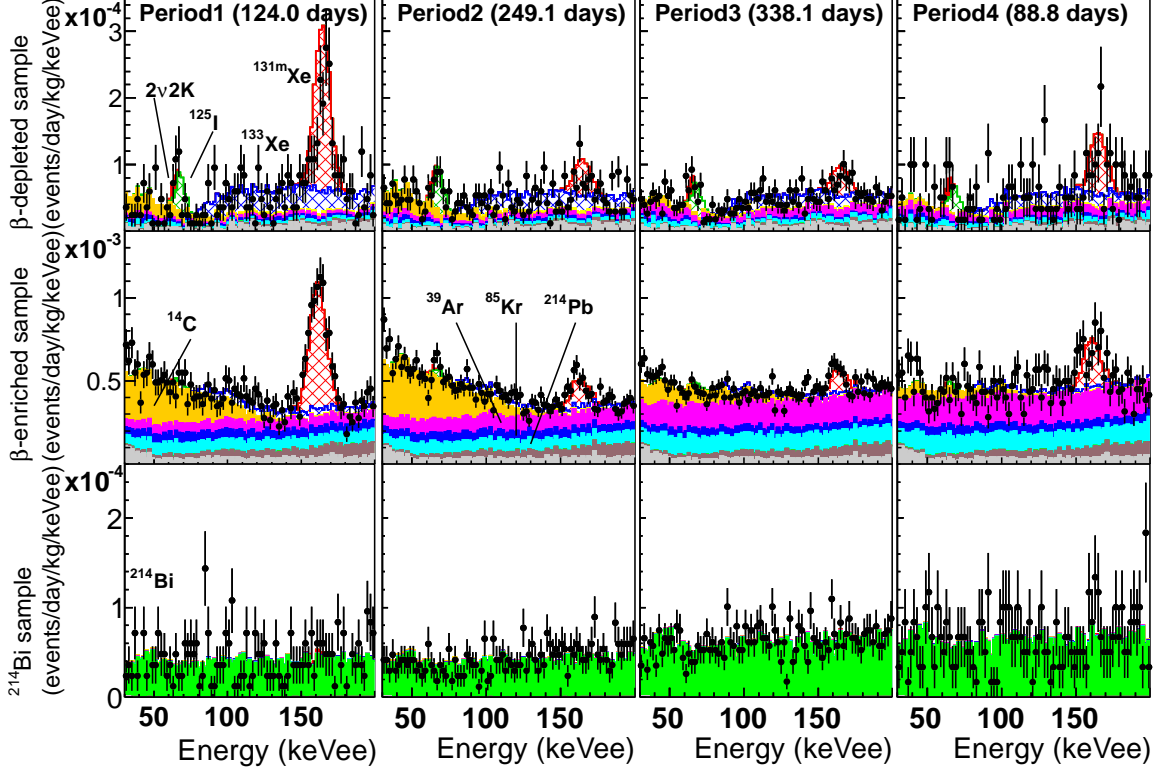


**Fig. 4** Energy spectra for the  $\beta$ -depleted samples (top),  $\beta$ -enriched samples (middle), and  $^{214}\text{Bi}$  samples (bottom). The observed data spectra (points) are overlaid with the best-fit  $2\nu 2K$  signal and background spectra (colored stacked histograms). Colored histograms are the  $2\nu 2K$  signal (red filled),  $^{125}\text{I}$  (green hatched),  $^{131\text{m}}\text{Xe}$  (red hatched),  $^{133}\text{Xe}$  (blue hatched),  $^{14}\text{C}$  (orange filled),  $^{39}\text{Ar}$  (magenta filled),  $^{85}\text{Kr}$  (blue filled),  $^{214}\text{Pb}$  (cyan filled),  $^{214}\text{Bi}$  (green filled),  $^{136}\text{Xe}$   $2\nu\beta\beta$  (brown filled), and external backgrounds (gray filled).

LXe outside the water shield and caused by the  $^{252}\text{Cf}$  calibrations. Increases in the  $^{133}\text{Xe}$  yield in periods 1 and 4 are not significant compared with the increases in the  $^{131\text{m}}\text{Xe}$  yield. The fitted energy scales for the  $\beta$ -enriched and the  $\beta$ -depleted samples vary within  $\pm 2\%$ , which is consistent with the evaluation before fitting.

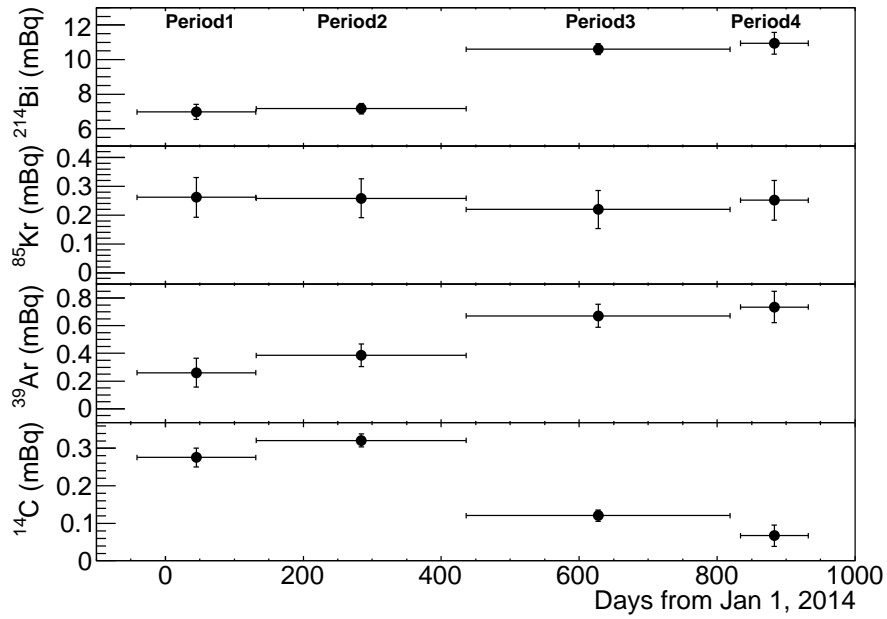
Closeup figures of energy spectra between 30 and 100  $\text{keV}_{\text{ee}}$  for the  $\beta$ -depleted samples are shown in Fig. 7. The peak found at 67.5  $\text{keV}_{\text{ee}}$  is attributable to the  $^{125}\text{I}$  decay. The event rate of the  $^{125}\text{I}$  decay is constrained by the thermal neutron flux.

Figure 8 shows the normalized profile likelihood  $L/L_{\text{max}}$  as a function of the inverse of the  $^{124}\text{Xe}$   $2\nu 2K$  half-life, where  $L_{\text{max}}$  is the maximum value of the likelihood. No significant excess over the expected background is found in the signal region. We calculate the 90% CL limit from the relation

$$\frac{\int_0^{\xi_{\text{limit}}} L(\xi) d\xi}{\int_0^{\infty} L(\xi) d\xi} = 0.9, \quad (6)$$

where  $\xi = 1/T_{1/2}^{2\nu 2K}$ . This leads to

$$T_{1/2}^{2\nu 2K} (^{124}\text{Xe}) > \frac{1}{\xi_{\text{limit}}} = 2.1 \times 10^{22} \text{ years}. \quad (7)$$



**Fig. 5** Time variation of the fitted activities of  $^{214}\text{Bi}$ ,  $^{85}\text{Kr}$ ,  $^{39}\text{Ar}$ , and  $^{14}\text{C}$  in the active 832 kg LXe volume. The left and right edges of the horizontal error bars represent the start and end of each period, respectively.

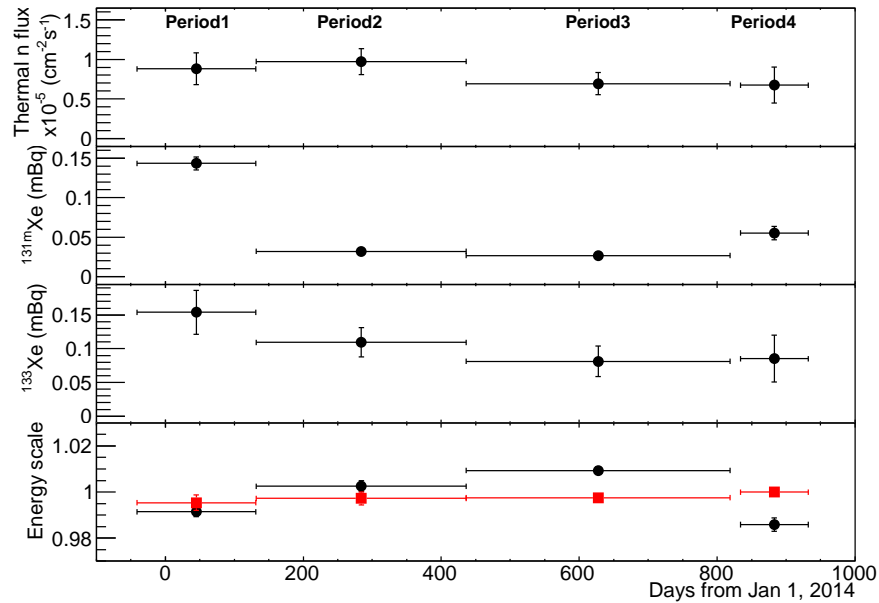


**Fig. 6** Time variation of the fitted thermal neutron flux, additional activities of  $^{131\text{m}}\text{Xe}$ ,  $^{133}\text{Xe}$  in the active 832 kg LXe volume, and energy scales for the  $\beta$ -enriched (black circle) and  $\beta$ -depleted samples (red rectangle). The left and right edges of the horizontal error bars represent the start and end of each period, respectively.

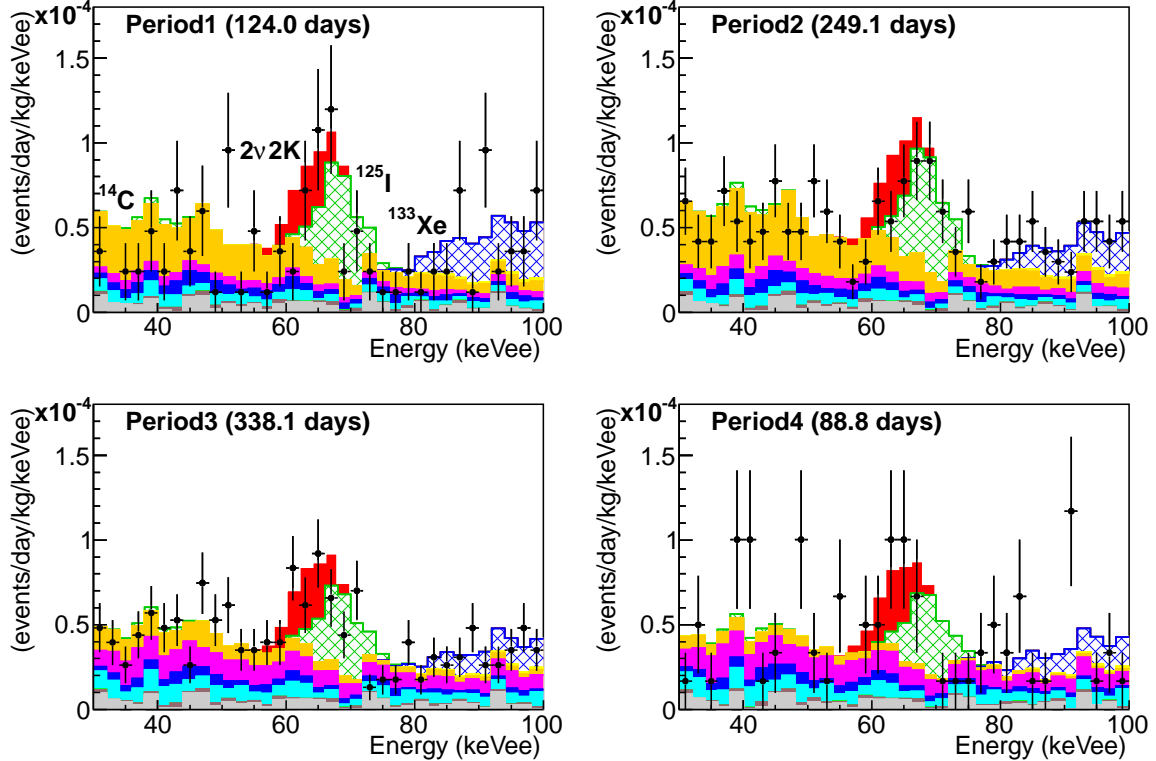


**Fig. 7** Closeup figures of energy spectra between 30 and 100 keV<sub>ee</sub> for the  $\beta$ -depleted samples. The observed spectra (points) are overlaid with the best-fit  $2\nu 2K$  signal and background spectra (colored stacked histograms). Colored histograms are the  $2\nu 2K$  signal (red filled),  $^{125}\text{I}$  (green hatched),  $^{133}\text{Xe}$  (blue hatched),  $^{14}\text{C}$  (orange filled),  $^{39}\text{Ar}$  (magenta filled),  $^{85}\text{Kr}$  (blue filled),  $^{214}\text{Pb}$  (cyan filled),  $^{136}\text{Xe}$   $2\nu\beta\beta$  (brown filled), and external backgrounds (gray filled).

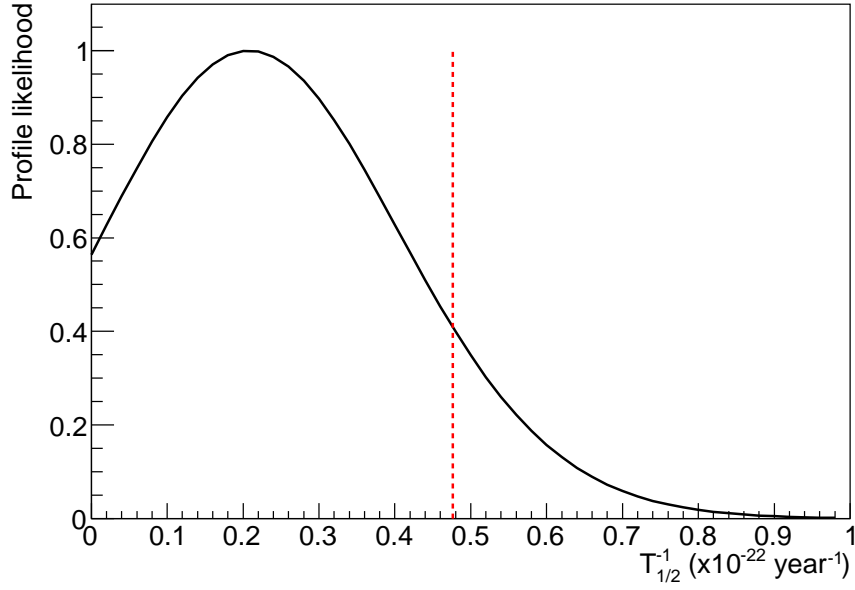
The fact that we do not observe significant excess above background allows us to give a constraint on  $2\nu 2K$  on  $^{126}\text{Xe}$  in the same manner:

$$T_{1/2}^{2\nu 2K} (^{126}\text{Xe}) > 1.9 \times 10^{22} \text{ years} \quad (8)$$

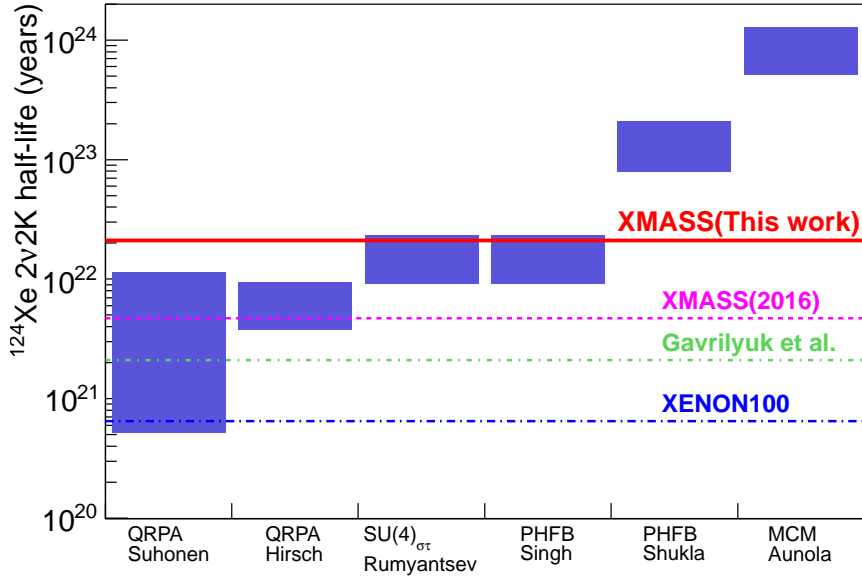
at 90% CL.

Figure 9 shows a comparison of the experimental 90% CL exclusion limits on  $^{124}\text{Xe}$   $2\nu 2K$  half-life overlaid with the theoretical calculations [21, 28–32] for comparison. The present result gives a lower limit stronger by a factor 4.5 over our previous result, and gives the most stringent experimental constraint reported to date. For the theoretical predictions, the reported  $2\nu\text{ECEC}$  half-lives are converted to  $2\nu 2K$  half-lives, divided by the branching ratio for the two electrons being captured from the  $K$ -shell,  $P_{2K}=0.767$  [54]. The lower and upper edges of the bands correspond to  $g_A = 1.26$  and  $g_A = 1$ , respectively.

Note that the predicted half-lives will be longer if quenching of  $g_A$  is larger. These experimental results rule out a part of the relevant range of the reported half-life predictions, and future experiments with multi-ton LXe targets will have improved sensitivity to further explore this parameter space.



**Fig. 8** Normalized profile likelihood  $L/L_{\max}$  as a function of the inverse of the  $^{124}\text{Xe}$   $2\nu 2\text{K}$  half-life. The vertical line indicates the 90% quantile from which the lower limit on the half-life is derived.



**Fig. 9** Comparison of the experimental 90% CL exclusion limits on the  $^{124}\text{Xe}$   $2\nu 2\text{K}$  half-life overlaid with the theoretical calculations [21, 28–32]. The lower and upper edges of the theoretical predictions correspond to  $g_A = 1.26$  and  $g_A = 1$ , respectively.

---

## 8. Conclusion

We have conducted an improved search for  $2\nu 2K$  on  $^{124}\text{Xe}$  and  $^{126}\text{Xe}$  using 800.0 days of data from XMASS-I. For this search, a novel method to discriminate  $\gamma$ -ray/ $X$ -ray or  $2\nu 2K$  signals from  $\beta$ -ray backgrounds using LXe scintillation time profiles was developed. With spectrum fitting in the energy range from 30 to 200 keV<sub>ee</sub>, no significant  $2\nu 2K$  signal appeared over the expected background. Therefore, we set the most stringent lower limits on the half-lives for these processes at  $2.1 \times 10^{22}$  years for  $^{124}\text{Xe}$  and  $1.9 \times 10^{22}$  years for  $^{126}\text{Xe}$  at 90% CL.

## Acknowledgements

We gratefully acknowledge the cooperation of the Kamioka Mining and Smelting Company. This work was supported by the Japanese Ministry of Education, Culture, Sports, Science and Technology, Grant-in-Aid for Scientific Research (19GS0204, 26104004, and 16H06004), the joint research program of the Institute for Cosmic Ray Research (ICRR), the University of Tokyo, and partially by the National Research Foundation of Korea Grant funded by the Korean Government (NRF-2011-220-C00006).

## References

- [1] R. G. Winter, Phys. Rev. **100**, 142 (1955).
- [2] M. Doi and T. Kotani, Prog. Theor. Phys. **89**, 139 (1993).
- [3] J. D. Vergados, Nucl. Phys. B **218**, 109 (1983).
- [4] J. Bernabeu, A. De Rujula, C. Jarlskog, Nucl. Phys. B **223**, 15 (1983).
- [5] Z. Sujkowski, S. Wycech, Phys. Rev. C **70**, 052501 (2004).
- [6] D. Frekers, hep-ex/0506002.
- [7] M. I. Krivoruchenko *et al.*, Nucl. Phys. A **859**, 140 (2011).
- [8] J. Kotila, J. Barea, F. Iachello, Phys. Rev. C **89**, 064319 (2014).
- [9] A. S. Barabash *et al.*, Nucl. Phys. A **785**, 371 (2007).
- [10] A. S. Barabash *et al.*, Phys. Rev. C **80**, 035501 (2009).
- [11] P. Belli *et al.*, Phys. Rev. C **87**, 034607 (2013).
- [12] P. Belli *et al.*, Nucl. Phys. A **930**, 195 (2014).
- [13] S. W. Finch and W. Tornow, Phys. Rev. C **92**, 065503 (2015).
- [14] M. Jeskovsky *et al.*, Nucl. Instrum. Meth. A **795**, 268 (2015).
- [15] G. Angloher *et al.*, J. Phys. G **43**, 095202 (2016).
- [16] M. Agostini *et al.*, Eur. Phys. J. C **76**, 652 (2016).
- [17] B. Lehnert *et al.*, J. Phys. G **43**, 065201 (2016).
- [18] B. Lehnert *et al.*, J. Phys. G **43**, 085201 (2016).
- [19] Y. M. Gavriluk *et al.*, Phys. Rev. C **87**, 035501 (2013).
- [20] W. C. Haxton, G. J. Stephenson, Prog. Part. Nucl. Phys. **12**, 409 (1984).
- [21] M. Hirsch *et al.*, Z. Phys. A **347**, 151 (1994).
- [22] A. P. Meshik *et al.*, Phys. Rev. C **64**, 035205 (2001).
- [23] M. Pujol *et al.*, Geochim. Cosmochim. Acta **73**, 6834 (2009).
- [24] S. S. Ratkevich *et al.*, Phys. Rev. C **96**, 065502 (2017).
- [25] S. M. Bilenky, C. Giunti, Int. J. Mod. Phys. A **30** 1530001 (2015).
- [26] J. T. Suhonen, Front. in Phys. **5**, 55 (2017).
- [27] M. Wang *et al.*, Chin. Phys. C **36**, 1603 (2012).
- [28] J. Suhonen, J. Phys. G **40** 075102 (2013).
- [29] O. A. Rumyantsev, M. H. Urin, Phys. Lett. B **443** 51 (1998).
- [30] S. Singh *et al.*, Eur. Phys. J. A **33** 375 (2007).
- [31] A. Shukla, P. K. Raina, P. K. Rath, J. Phys. G **33** 549 (2007).
- [32] M. Aunola, J. Suhonen, Nucl. Phys. A **602** 133 (1996).
- [33] Y. M. Gavriluk *et al.*, Phys. Part. Nucl. **46**, 147 (2015).
- [34] Y. M. Gavriluk *et al.*, Phys. Part. Nucl. **48**, 38 (2017).
- [35] D.-M. Mei *et al.*, Phys. Rev. C **89**, 014608 (2014).
- [36] N. Barros, J. Thurn, K. Zuber, J. Phys. G **41**, 115105 (2014).
- [37] K. Abe *et al.* (XMASS Collaboration), Phys. Lett. B **759**, 64 (2016).
- [38] E. Aprile *et al.* (XENON Collaboration), Phys. Rev. C **95**, 024605 (2017).
- [39] K. Abe *et al.* (XMASS Collaboration), Nucl. Instrum. Meth. A **716**, 78 (2013).



- 
- [40] N. Y. Kim *et al.* (XMASS Collaboration), Nucl. Instrum. Meth. A **784**, 499 (2015).
- [41] S. Guatelli *et al.*, IEEE Trans. Nucl. Sci. **54**, 585 (2007);  
S. Guatelli *et al.*, IEEE Trans. Nucl. Sci. **54**, 594 (2007).
- [42] D. A. Nesterenko *et al.*, Phys. Rev. C **86**, 044313 (2012).
- [43] R. B. Firestone *et al.*, *Table of Isotopes*, John Wiley & Sons, Inc., New York, 8 ed., 1998.
- [44] T. Doke *et al.*, in Proceedings of the International Workshop on Technique and Application of Xenon Detectors (Xenon 01), World Scientific, 17 (2003).
- [45] H. Takiya *et al.* (XMASS Collaboration), Nucl. Instrum. Meth. A **834**, 192 (2016).
- [46] K. Fujii *et al.*, Nucl. Instrum. Meth. A **795**, 293 (2015).
- [47] R. A. Fisher, *Statistical Methods for Research Workers*, Oliver & Boyd, 14th ed., 1970.
- [48] K. Abe *et al.* (XMASS Collaboration), arXiv:1804.02180 [astro-ph.CO].
- [49] J. B. Albert *et al.* (EXO-200 Collaboration), Phys. Rev. C **89**, 015502 (2014).
- [50] A. Gando *et al.* (KamLAND-Zen Collaboration), Phys. Rev. Lett. **117**, 082503 (2016).
- [51] S. F. Mughabghab, INDC(NDS)-440, 2003.
- [52] A. Minamino, Master thesis, the University of Tokyo (2004).
- [53] W. Ootani, Master thesis, the University of Tokyo (1994).
- [54] M. Doi and T. Kotani, Prog. Theor. Phys. **87**, 1207 (1992).